2026 IEEE International Conference on Robotics and Automation (ICRA 2026)
June 1-5, 2026. Vienna, Austria

Physics-Based Reduced-Order Modeling of Magnetic Microparticle Swarms for Biomedical Control

Fadalallah Boudehane[1], Lyès Mellal[1], Trung Son Do[1], David Folio[1], Antoine Ferreira[1]

***Abstract*— Magnetic particle swarms are governed by rich nonlinear collective dynamics that complicate predictive, feedback-based control in biomedical microrobotics. We develop a physics-based reduced-order ellipse model that describes the swarm morphology by its principal radii (r_1, r_2). At steady state, these radii depend explicitly on magnetic-field curvature, axial gradients, and actuation angular velocity through anisotropic stiffness terms. Model parameters are identified experimentally, yielding low validation errors (RMSE: 0.25 mm for r_1 and 0.42 mm for r_2) and revealing pronounced stiffness anisotropy ($S_x/S_y \approx 0.16$). The resulting formulation provides compact, interpretable equations that enable tractable control design and feedback regulation of magnetic particle swarms.**

I. INTRODUCTION

Magnetic control of micro- and nano-particle swarms has emerged as a promising strategy for minimally invasive biomedical applications such as microsurgery [1], hyperthermia [2], and targeted drug delivery [3]. By applying external magnetic fields, it is possible to induce diverse collective behaviors in particle ensembles suspended in fluids, including aggregation, dispersion, translation, and rotation [4]. Compared to single-agent microrobots, swarms offer advantages in scalability, robustness, and fault tolerance in complex environments where individual manipulation may be impractical [5]–[7].

Despite these advantages, achieving precise and automated control of swarm behavior remains challenging. Swarm dynamics are highly nonlinear, arising from dipole–dipole interactions, hydrodynamic coupling, applied magnetic fields, and external disturbances. Variations in actuation parameters such as magnet position or rotation frequency induce diverse morphologies, including ellipsoidal clusters, rod-like aggregates, and multi-vortex states. Previous studies have investigated how rotating magnetic fields generate such patterns: Yu et al. [6] related vortex size and shape to driving frequency and field strength; Kokot and Snezhko [7] reported macroscopic vortices in magnetic rollers; and Petricenko et al. [8] quantified swarm size and angular velocity in hematite cubes. Related collective pattern formation under rotating magnetic actuation has also been reported for spinning magnetic micro-disks without an explicit focus on control-oriented modeling [10].

*This work was funded by the Centre-Val de Loire Region under the CatheterBot project (Regional Interest Research Project – JCJC, agreement no. 2022-00150406), and project ANR MAGOA (ANR-23-CE33-0007-01).

[1] All authors are with INSA CVL, Université d'Orléans, PRISME UR 4229, Bourges, France. (Contact: fadal.boudehane@insa-cvl.fr,david.folio@insa-cvl.fr, antoine.ferreira@insa-cvl.fr)

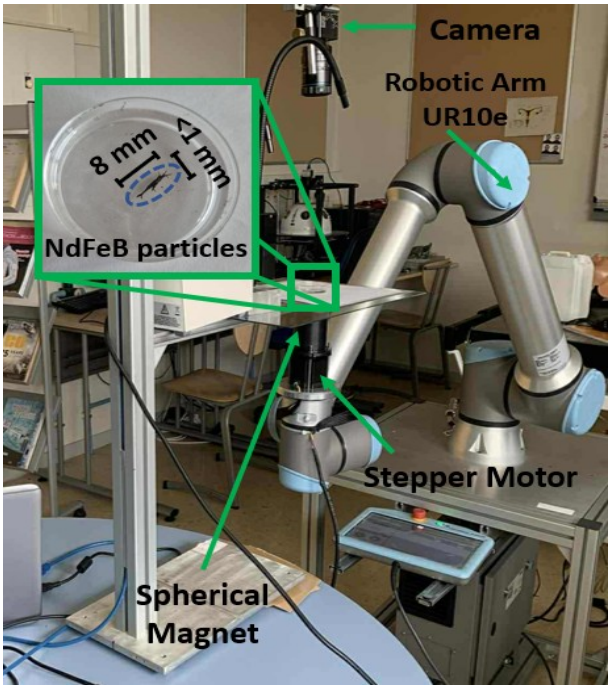

Fig. 1: Experimental setup: UR10e robotic arm with a spherical magnet with a radius of 20*mm*, camera, and acquisition system.

Several modeling and control frameworks have been developed to address swarm coordination. Yang et al. [11] demonstrated feedback control of magnetic collectives, Xie et al. [12] introduced reconfigurable multimode strategies, Dong and Sitti [13] extended control to cooperative 2D formations, and Chaluvadi et al. [16] proposed a covariance-based kinematic model. Although these studies advanced swarm control and characterization, they do not provide explicit parametric descriptors that relate swarm morphology to magnetic-field conditions, particle interactions, and fluid effects. Dimensionless quantities such as the Mason number partially capture the balance between viscous and magnetic forces [14], [24], but they remain insufficient for predictive closed-loop control, which requires compact, physics-grounded reduced-order formulations [13]–[15].

Recently, computer vision and AI-based methods have been developed to characterize swarm morphology and transitions in real time. Tang et al. [17] demonstrated real-time AI control of nanoparticle collectives, Jiang et al. [18] applied deep learning for adaptive swarm navigation, and Xia et al. [19] introduced a physics-assisted AI framework

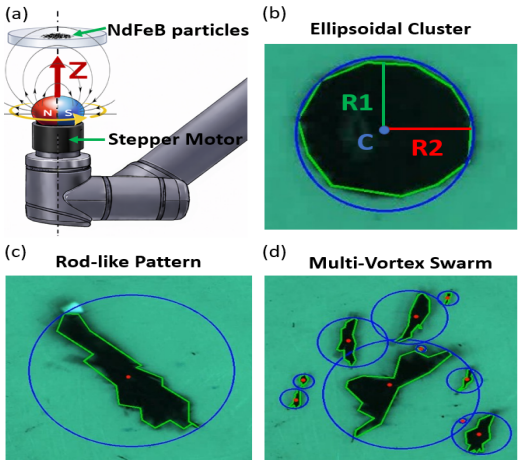

Fig. 2: (a) Stepper-driven spherical NdFeB magnet mounted on the robotic arm, generating a controlled rotating dipole field (figure generated using OpenAI's ChatGPT); and Swarm morphologies: (b) ellipsoidal cluster, (c) rod-like pattern, and (d) multi-vortex swarm formed by magnetic microparticles under actuation.

capable of predicting multimodal swarm behaviors under programmable fields. Although these approaches are powerful for monitoring and classification, they often lack physical interpretability or direct links to governing equations. This motivates the need for hybrid frameworks; physics-based models that are compact enough for control while capturing essential swarm features, and which can later be integrated with AI for adaptability [20].

In this work, we develop a phenomenological reduced-order model to predict the steady-state morphology of magnetic particle swarms. In contrast to particle-level models, which are nonlinear and parameter-varying, the proposed formulation yields compact, physics-grounded equations suitable for control. We consider neodymium–iron–boron (NdFeB) particles actuated by a spherical permanent magnet mounted on a robotic arm [21], [22], forming stable ellipsoidal clusters relevant to biomedical applications [4], [23]. The model is validated through closed-loop simulations with MIMO PID tracking and open-loop experiments, showing good agreement with measured swarm morphologies and enabling predictive feedback regulation.

This article is organized as follows. Section II presents the reduced-order ellipse model and its parametric structure. Section III describes the experimental setup, swarm phenomenology, and model validation. Section IV addresses limitations, extensions to multimodal dynamics, and biomedical implications. Finally, Section V summarizes the main findings.

II. Modeling Framework

A. Model Formulation

At the particle level, swarm behavior arises from nonlinear dipole–dipole interactions, hydrodynamic drag, confinement, and stochastic effects [9], [12]. Although qualitatively understood, the resulting many-body dynamics prevent closed-form analytical descriptions at the collective scale. We therefore adopt a phenomenological reduced-order representation, motivated by the rapid self-organization of particles into cohesive clusters observed experimentally. The cluster footprint can be approximated by an ellipse with principal radii r_1 and r_2 (Fig. 2b), which serve as low-dimensional descriptors of in-plane morphology. This abstraction enables tractable parameter identification and control design while retaining essential physical dependencies.

To simplify the reduced-order description, we adopt the following assumptions :

1) The swarm centroid coincides with the center of the applied rotating magnetic field. 2) The swarm envelope rotates at the same angular velocity as the applied field ($\omega_{\text{swarm}} = \omega_m$). In the following, experimental actuation is specified in terms of the frequency f_m(Hz), while the model uses ω_m. 3) Out-of-plane deformations are neglected, and the swarm footprint is described solely by its in-plane principal radii r_1 and r_2.

These assumptions are consistent with prior studies of rotating-field-driven particle ensembles [6], [14], and allow the model to capture the dominant morphology dynamics while remaining tractable for control-oriented analysis.

The time evolution of r_1 and r_2 arises from three dominant mechanisms:

a) Magnetic confinement: Dipole alignment and field gradients pull particles toward the centroid, producing anisotropic contraction. We approximate the confinement strength along axis $i \in \{1,2\}$ as

$$F_{B,i}(r_i; z_m) = K_{b,i}\, S_i(z_m)\, (r_i - r_{i,\min})^{\beta}, \tag{1}$$

where $r_{i,\min}$ is the particle-packing limit, β adjusts the nonlinearity of confinement, and $S_i(z_m)$ is an anisotropic stiffness function derived from field curvature and gradients at the swarm–field distance z_m. Here, $K_{b,i} > 0$ is an axis-specific confinement gain that scales the contribution of the anisotropic stiffness.

b) Rotation-driven expansion: The rotating field induces centrifugal and shear stresses that act collectively to enlarge the footprint. This effect is modeled phenomenologically as

$$\mathscr{E}(r_1, r_2; z_m, \omega_m) = K_\tau \left(\frac{|\omega_m|}{\omega_{\text{ref}}}\right)^{p} s_B\, B(z_m)\, (r_1\, r_2), \tag{2}$$

with ω_m the angular frequency of the field, $\omega_{\text{ref}} = 2\pi f_{\text{ref}}$ a reference angular frequency, $B(z_m)$ the field magnitude, and (K_τ, p, s_B) fitted coefficients. The multiplicative term $(r_1 r_2)$ is indicative of the empirical observation that larger footprints experience proportionally greater shear expansion.

c) Linear relaxation: Effective dissipative relaxation of the swarm envelope arises from fluid-mediated dissipation and internal particle rearrangements. We model this behavior using a first-order relaxation term

$$D_i(r_i) = K_{d,i}\, r_i, \tag{3}$$

where $K_{d,i}$ aggregates viscous and stochastic contributions to the damping of envelope dynamics.

By combining expressions (1), (2), and (3), the following reduced-order system is obtained:

$$\begin{aligned}\dot{r}_1 =& -K_{b,1}S_x(z_m)(r_1 - r_{1,\min})^{\beta} + \mathscr{E}(r_1, r_2; z_m, \omega_m) \\ & - K_{d1}r_1, \\ \dot{r}_2 =& -K_{b,2}S_y(z_m)(r_2 - r_{2,\min})^{\beta} + \mathscr{E}(r_1, r_2; z_m, \omega_m) \\ & - K_{d2}r_2,\end{aligned} \tag{4}$$

where S_x, S_y are anisotropic stiffness functions reflecting asymmetries of the rotating magnetic field.

B. Physics-Based Reduced-Order Model

Under steady-state conditions ($\dot{r}_i = 0$), Eq. (4) expresses a balance between magnetic confinement, effective dissipative relaxation, and rotation-induced expansion at the swarm-envelope level. Although this balance defines the steady morphology, the resulting coupled nonlinear relations provide limited analytical insight and are ill-suited for parameter identification and control design. Guided by the structure of Eq. (4) and supported by experimental observations, we therefore reformulate the steady-state relation into a physics-based empirical parametric model as follows:

$$\begin{aligned} r_1(z_m, \omega_m) &= \frac{C_1\,\Phi(\omega)}{S_x(z_m, \omega_m)^{\alpha_1}}, \\ r_2(z_m, \omega_m) &= \frac{C_2\,\Phi(\omega)}{S_y(z_m, \omega_m)^{\alpha_2}}, \end{aligned} \tag{5}$$

where C_1, C_2 are axis-specific gains, and α_1, α_2 are nonlinear exponents capturing the sensitivity of each axis.

The frequency-dependent term is expressed as

$$\Phi(\omega_m) = \exp\left[N\left(\left(\frac{|\omega_m|}{\omega_{\text{ref}}}\right)^{q} - 1\right)\right], \tag{6}$$

where N and q tune how rotation amplifies expansion relative to the reference frequency.

The anisotropic stiffness functions combine curvature, gradient, and interparticle effects as defined in (7):

$$\begin{aligned} S_x(z_m, \omega_m) &= s_0 + a_{K1}\,|k_{xx}^{(B^2)}(z_m)|^{\gamma_1} + a_G\, g_z(z_m)^{\rho} \\ &\quad + a_P\left(\frac{B(z_m)}{B_{\text{ref}}}\right)^{\mu_P}\left[1 + \log\left(1 + c_P\left(\frac{|\omega_m|}{\omega_{\text{ref}}}\right)^{q_P}\right)\right], \\ S_y(z_m, \omega_m) &= s_0 + a_{K2}\,|k_{yy}^{(B^2)}(z_m)|^{\gamma_2} + a_G\, g_z(z_m)^{\rho} \\ &\quad + a_P\left(\frac{B(z_m)}{B_{\text{ref}}}\right)^{\mu_P}\left[1 + \log\left(1 + c_P\left(\frac{|\omega_m|}{\omega_{\text{ref}}}\right)^{q_P}\right)\right]. \end{aligned} \tag{7}$$

Here, s_0 denotes the baseline stiffness; a_{K1}, a_{K2} are curvature gains with exponents γ_1, γ_2; a_G and ρ scale the axial gradient $g_z(z_m)$; and particle–interaction effects are captured by a_P, μ_P with normalization by B_{ref}. The coefficient c_P with exponent q_P accounts for frequency–field interactions. The curvature terms $k_{xx}^{(B^2)}$ and $k_{yy}^{(B^2)}$ correspond to second derivatives of the squared magnetic field along x and y, and are included to account for confinement and shape stability effects that cannot be captured by field magnitude or gradients alone. $B(z_m)$ is the field magnitude at height z_m.

The logarithmic term in (7) captures the gradual weakening of interparticle cohesion with increasing rotation frequency. It modulates particle–particle interactions without suppressing them at low frequency and remains well-behaved over the actuation range (1–10 Hz). This term accounts for frequency-dependent rotational effects observed at the particle level.

From a control perspective, the resulting anisotropic stiffness functions determine the relative sensitivity of the principal radii to actuation inputs, thereby shaping the achievable aspect ratio and conditioning of feedback control along each axis. By construction, $S_x, S_y > 0$ due to numerical flooring, ensuring physically meaningful stiffness values.

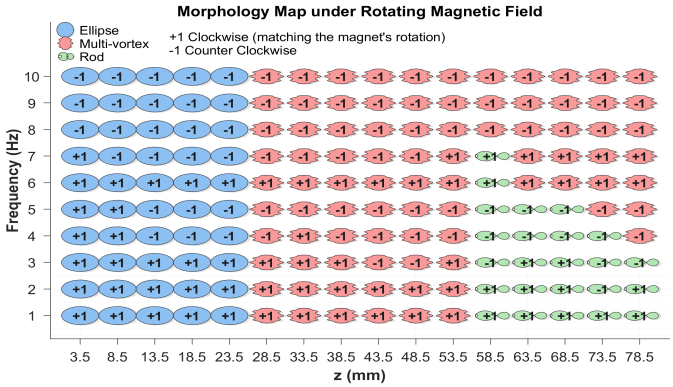

Fig. 3: Experimental morphology map of magnetic particle swarms under a rotating spherical magnet.

III. Experimental Validation

A. System Description

Our experimental platform (Fig. 1) combines a 6-DoF UR10e manipulator (Universal Robots e-Series, Odense, Denmark) with a stepper-driven spherical NdFeB magnet of radius 20 mm (Fig. 2a). The stepper motor provides continuous rotation, generating a controlled rotating dipole field, while the manipulator moves the magnet along the z-axis.

The magnetic flux density of the sphere was characterized using a 3D Hall sensor array at varying distances, and the equivalent dipole moment $|\mathbf{M}|$ was estimated by least-squares fitting to a point-dipole model.

The swarms were formed from NdFeB microparticles (MQFP 15-7, Magnequench Inc.) with a mean diameter of 5 µm. The experiments were carried out in a cylindrical water reservoir of radius 53 mm ($\rho = 997$ kg/m^3, $\eta = 0.890$ mPa·s). Swarm footprints in the imaging plane were tracked with an EXO174CU3 industrial camera (SVS-Vistek GmbH, Germany).

System control was implemented in ROS2 Humble using the Universal Robots driver, enabling real-time execution of preprogrammed Cartesian trajectories.

TABLE I: Identified Parameters and Validation Errors.

Axis-Specific Parameters	r_1	r_2
C_i [mm]	7.76	16.6
$a_{K,i}$ [–]	0.487	2.58
α_i [–]	0.10	0.45
γ_i [–]	0.21	0.10
Global Parameters	Values	
s_0 [–]	0.023	
a_G [–]	0.20	
N, q [–]	$-0.273, 0.24$	
a_P, μ_P [–]	$0.823, 0.33$	
c_P, q_P [–]	$-0.77, 0.10$	
f_{ref} [Hz]	6	
Validation Errors [a]	r_1	r_2
RMSE [mm]	0.248	0.415
MAE [%]	6.49	9.12
Median Stiffness	S_x	S_y
Value [–]	0.393	2.455

[a]RMSE and MAE are computed over all experimental conditions, while median stiffness values summarize the fitted S_x and S_y functions.

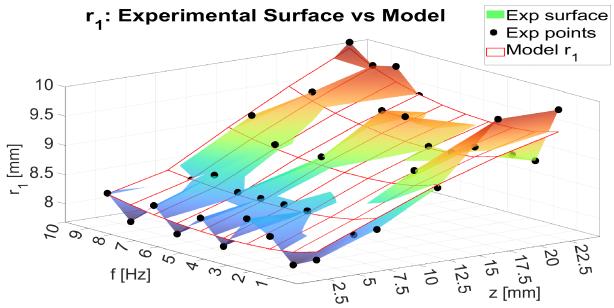

(a)

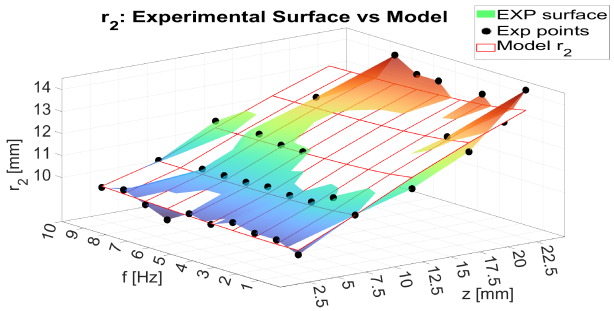

(b)

Fig. 4: Comparison between experimental data and model predictions for swarm radii: (a) r_1, (b) r_2.

B. Swarm Morphologies

When subjected to a rotating magnetic field, ensembles of NdFeB microparticles in fluid self-organize into collective morphologies. The dependence of these morphologies on the magnet's vertical position (z_m) and frequency (f_m) is summarized in the morphology map (Fig. 3), which highlights well-defined domains of ellipsoidal clusters, rod-like patterns, and multi-vortex swarms, as well as the frequency-dependent inversion of rotation direction.

At low f_m and small z_m, particles condense into compact aggregates aligned with the field. Increasing f_m elongates these aggregates into ellipsoidal clusters (Fig. 2b), whose aspect ratio grows systematically with frequency and magnet position. Notably, below a critical cutoff frequency $f_{\text{off}} \approx 6$ Hz, the swarm co-rotates with the magnetic field, while above this frequency, it rotates in reverse direction. This inversion reflects a viscous phase lag that dominates the dipolar alignment at higher frequencies.

At larger z_m, magnetic coupling weakens and swarm coherence diminishes. Beyond a threshold $z_{\text{off}} \approx 23.5$ mm, ellipsoidal clusters are no longer sustained and the swarm transitions to multi-vortex states (Fig. 2d), where smaller vortices rotate locally. Rod-like aggregates (Fig. 2c) appear in intermediate regimes but remain unstable. For $28.5 \leq z_m \leq 53.5$ mm, multi-vortex behavior dominates, indicating that reduced magnetic gradients favor fragmentation over elongation. This transition is consistent with the Mason number framework [14], where increasing viscous-to-magnetic stress promotes fragmentation.

Among the different morphologies, the ellipsoidal state is particularly attractive for biomedical applications, as it provides an elongated yet coherent footprint that can be steered precisely while maintaining structural connectivity.

C. Model Validation and Analysis

After parameter identification, the reduced-order ellipse model was validated against the full experimental dataset of 50 operating points spanning magnet–swarm distances ($z_m \in [3.5, 23.5]$ mm) and frequencies ($f_m \in [1, 10]$ Hz). For each point, 10 repeated measurements of the radii (r_1, r_2) were collected; mean values were used for identification, and variability was quantified by standard deviation and median absolute deviation. Parameters were estimated via nonlinear least-squares fitting to minimize the root mean square error (RMSE) between experimental means and model predictions. The fitted parameters and error metrics are reported in Table I.

a) Agreement across (z_m, f_m): The 3D surfaces of r_1 and r_2 reveal three main trends (Fig. 4): (i) increasing z_m enlarges both radii, reflecting weaker magnetic gradients and reduced confinement; (ii) at low f_m, the radii decrease with frequency due to stronger viscous alignment; (iii) at higher f_m, both radii increase again as rotation-induced expansion dominates. The model captures this non-monotonic frequency dependence together with the distance effect. Axis anisotropy is also reproduced, with r_2 consistently larger than r_1, consistent with preferential head–to–tail chaining along field lines. Ridge and valley structures align closely between model and experiments, with only minor deviations at the workspace boundaries (largest z_m, highest f_m), where cohesion weakens.

b) Axis-dependent variability: Experimentally, r_2 exhibits greater run-to-run variability than r_1, particularly at intermediate (z_m, f_m). This is consistent with the stiffness

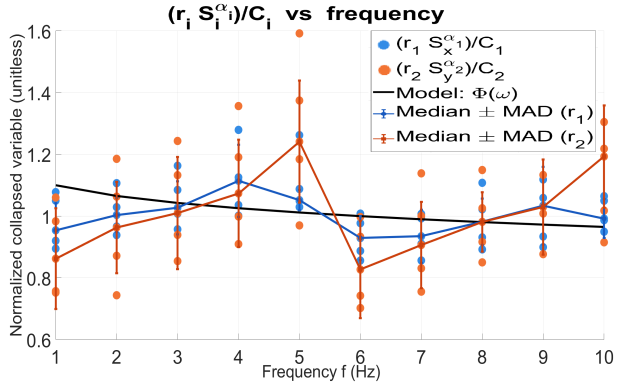

Fig. 5: Collapsed frequency response of swarm radii (r_1, r_2) via dimensionless scaling.

structure: along the field-aligned axis (y), dipole chains couple more strongly to magnetic curvature but are also more sensitive to centrifugal and shear effects, resulting in both larger mean values and increased variance. The model captures this anisotropic scaling while attenuating high-frequency scatter, in line with its quasi-steady formulation.

c) Collapsed representation: To test separability, we define collapsed variables $y_i = (r_i S_i^{\alpha_i})/C_i$, $i \in \{1,2\}$, where r_i are the experimental values, which should collapse to the frequency curve $\Phi(\omega) = \exp\{N[(|\omega|/\omega_{\text{ref}})^q - 1]\}$. As shown in Fig. 5, both axes cluster around the same slowly decreasing trend. Median values (Median $\pm$ MAD) track $\Phi(\omega)$ within 5–10% across most bins. The main deviations occur near $f_m \approx 5$–6 Hz (retrograde transition) and at the highest frequency, where weak cohesion amplifies variability. Since the model uses $|\omega|$ and omits phase/step-out effects, small biases at these points are expected.

d) Stiffness anisotropy: Although the squared field curvature is nearly isotropic ($k_{xx}/k_{yy} \approx 1.04$), the fitted stiffness values show strong anisotropy ($S_x/S_y \approx 0.16$). This reflects the stronger alignment and cohesion of head-to-tail dipole chains along r_2, yielding larger radii but also greater sensitivity to shear and centrifugal forces (range 5.66 mm). In contrast, side-by-side configurations along r_1 provide weaker cohesion and higher drag, leading to smaller, more stable footprints (range 2.02 mm).

e) Take-away: Overall, the model achieves sub-millimeter accuracy (RMSE: 0.25 mm for r_1, 0.42 mm for r_2; MAE: 6.5% and 9.1%). It captures geometry, anisotropy, and frequency scaling, while the collapsed analysis supports the separable parametric structure. The deviations mainly arise near retrograde rotation and weak-cohesion regimes, motivating future inclusion of phase dynamics.

D. Reference Tracking

a) Tracking performance: Fig. 6 shows the radii tracking results with a simulated MIMO PID controller. With tuned gains, the controller tracks $r_1 : 7 \to 8 \to 9$ mm while holding $r_2 = 11$ mm. The model predictions were $r_1 = 7.61, 8.14, 8.50$ mm and $r_2 = 10.43, 11.23, 11.70$ mm, respectively. Across the three representative operating points,

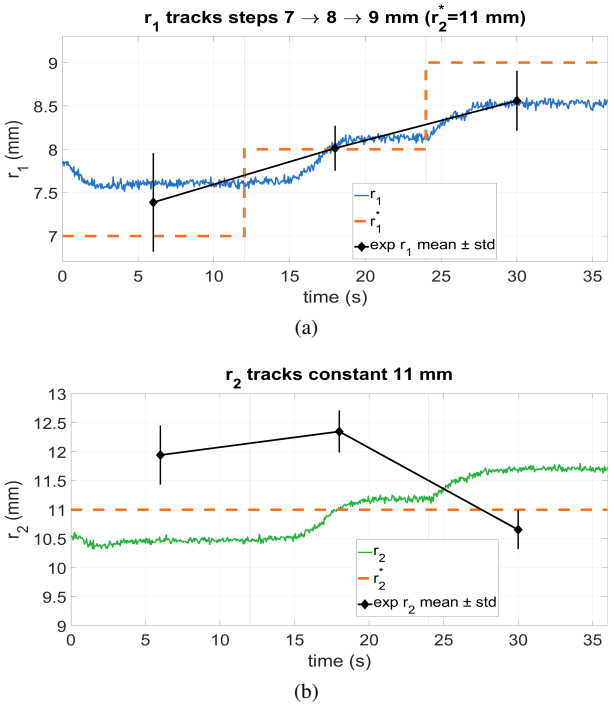

Fig. 6: Comparison between model predictions (closed-loop PID control) and experimental measurements (open-loop) of the swarm radii. In the experiments, (a) the target along the x-axis was varied in steps $r_1^* = 7 \to 8 \to 9$ mm, while (b) the target radius along the y-axis was fixed to $r_2^* = 11$ mm.

the model achieves sub-millimeter accuracy for r_1 (RMSE $=$ 0.25–0.63 mm, MAE $= 2\%$–9%) and for r_2 (RMSE $= 0.29$–0.66 mm, MAE $= 2\%$–6%), without sustained saturation.

b) Experimental comparison: Open-loop experiments at fixed (z_m, f_m) yielded mean radii of $\langle r_1 \rangle = 7.39 \pm 0.57$ mm, 8.01 ± 0.26 mm, and 8.56 ± 0.35 mm; and $\langle r_2 \rangle = 11.94 \pm 0.51$ mm, 12.35 ± 0.36 mm, and 10.65 ± 0.33 mm across the three setpoints. The alignment with the simulated trajectories confirms that, under the same actuation, the reduced-order model predicts radii within the experimental spread, with an underestimation of r_2 by about 1–1.5 mm. A supplementary video illustrates the reference-tracking experiments.

c) Sources of discrepancy: Remaining mismatches arise from the open-loop variability of the swarm—particularly along r_2—and from the proximity to the frequency offset $f_{\text{off}} \approx 6$ Hz, where rotation reversal and phase lag are not captured by the current model.

IV. Discussion

The proposed reduced-order ellipse model compresses the complexity of swarm morphology into two physically interpretable descriptors, the principal radii r_1 and r_2. By linking these observables to magnetic field curvature, gradients, and frequency-dependent amplification, the model provides a compact and physics-grounded framework for describing steady-state swarm footprints.

a) Predictive performance: The model demonstrates consistent predictive accuracy across experimental conditions, with RMSE of 0.25 mm for r_1 and 0.42 mm for r_2. The frequency-dependent amplification $\Phi(\omega)$ captures the nonlinear effect of rotation, while the stiffness functions S_x, S_y reflect spatial variations of field curvature and gradients. Importantly, the fitted parameters reveal a marked anisotropy ($S_x/S_y \approx 0.16$), consistent with stronger chaining of dipoles along the r_2 axis. This explains why swarms elongate preferentially along one axis while remaining more compact orthogonally.

b) Limitations: Several simplifications limit the current formulation. First, the steady-state assumption neglects transient dynamics such as formation time, oscillations, and vortex merging. Second, the use of $|\omega|$ ignores the experimentally observed inversion of swarm rotation above $f_{\text{off}} \approx 6$ Hz. Although footprint size depends mainly on $|\omega|$, omitting directionality and phase-lag effects introduces systematic errors near this transition. Finally, the reduced-order model abstracts away particle-level heterogeneity, hydrodynamic coupling, and confinement effects, which may become important in more complex environments.

c) Strengths and relevance: Despite these limitations, the model provides a compact, physically grounded, and interpretable description of swarm morphology. Its explicit parametric structure links magnetic-field curvature, axial gradients, field intensity, and actuation frequency to the steady-state footprint, revealing the mechanisms underlying anisotropic stiffness and frequency-driven expansion. Consequently, the model is particularly well suited for control-oriented applications requiring validated, low-dimensional, and computationally tractable formulations.

V. Conclusion

We presented a reduced-order ellipse model for predicting swarm morphology under rotating magnetic fields. The model captures anisotropic stiffness and frequency-dependent expansion with low prediction error, providing a compact and physically interpretable foundation for control. Although restricted to steady-state ellipsoidal clusters, it is well suited for feedback regulation and control-oriented analysis. Future work will extend the framework to quasi-steady and mode-aware dynamics, and explore in-vitro biomedical scenarios and hybrid physics–AI approaches for enhanced robustness in closed-loop control.

Acknowledgments

The authors acknowledge the use of OpenAI's ChatGPT for assistance in text editing and restructuring, specifically in improving clarity and readability of certain sections of the manuscript. In addition, Fig. 2(a) was generated using OpenAI's ChatGPT based on a real image and a textual description provided by the authors.

References

[1] Nelson, B. J., Kaliakatsos, I. K.,& Abbott, J. J. Microrobots for minimally invasive medicine. Annu. Rev. Biomed., 12, 55–85, 2010. DOI: 10.1146/annurev-bioeng-010510-103409

[2] Johannsen, M., Gneveckow, U., Taymoorian, K., et al. Magnetic nanoparticle hyperthermia for prostate cancer Int. j. hypertherm., 26(7), 790–795, 2010. DOI: 10.3109/02656731003745740

[3] Yu, J., Esteban-Fernández de Ávila, B., Gao, W., et al. Active generation and magnetic actuation of microrobotic swarms in bio-fluids Nat. Commun., 10, 2720, 2019. DOI: 10.1038/s41467-019-13576-6

[4] Chen, H., Yu, J. Magnetic Microrobotic Swarms in Fluid Suspensions. Curr. Robot Rep., 3, 127–137 (2022). DOI: 10.1007/s43154-022-00085-6

[5] K. Abolfathi, M. R. H. Yazdi and A. K. Hoshiar, "Studies of Different Swarm Modes for the MNPs Under the Rotating Magnetic Field," in IEEE Trans. Nanotechnol., vol. 19, pp. 849-855, 2020, doi: 10.1109/TNANO.2020.3041798.

[6] Yu, J., Yang, L.,& Zhang, L. Pattern generation and motion control of a vortex-like paramagnetic nanoparticle swarm. Int. J. Robot. Res., 37(8), 912–930, 2018. DOI: 10.1177/0278364918784366

[7] Kokot, G.,& Snezhko, A. Manipulation of emergent vortices in swarms of magnetic rollers. Nat. Commun., 9, 2344, 2018. DOI: 10.1038/s41467-018-04765-w

[8] Petricenko, O., et al. Swarming of micron-sized hematite cubes in a rotating magnetic field – Experiments. Journal of Magnetism and Magnetic Materials, 500, 166404, 2020. DOI: 10.1016/j.jmmm.2020.166404

[9] E. M. Purcell; Life at low Reynolds number. Am. J. Phys. 1 January 1977; 45 (1): 3–11. DOI: 10.1119/1.10903

[10] Wendong Wang et al. ,Order and information in the patterns of spinning magnetic micro-disks at the air-water interface.Sci. Adv.8,eabk0685(2022).DOI:10.1126/sciadv.abk0685

[11] Lidong Yang and Li Zhang Motion Control in Magnetic Microrobotics: From Individual and Multiple Robots to Swarms IEEE Trans. Robot., 31(1), 117–127, 2015. DOI: 10.1109/TRO.2014.2363634

[12] Xie, H., Sun, M., Fan, X., et al. Reconfigurable magnetic microrobot swarm: Multimode transformation, locomotion, and manipulation. Sci. Robot., 4(28), eaav8006, 2019. DOI: 10.1126/scirobotics.aav8006

[13] Dong, X.,& Sitti, M. Controlling two-dimensional collective formation and cooperative behavior of magnetic microrobot swarms. Int. J. Robot. Res., 39(5), 617–638, 2020. DOI: 10.1177/0278364920903107

[14] Bente, K., Reuter, D.,& Fischer, P. Selective actuation and tomographic imaging of swarming magnetite nanoparticles. ACS Applied Nano Materials, 4(7), 6752–6759, 2021. DOI: 10.1021/acsanm.1c01228

[15] Yang, L., Yu, J., Wang, B., Nelson, B. J.,& Zhang, L. A Survey on Swarm Microrobotics. IEEE Trans. Robot., 37(6), 1739–1759, 2021. DOI: 10.1109/TRO.2021.3111788

[16] Chaluvadi, B. K., Stewart, K. M., Sperry, A. J., Fu, H. C.,& Abbott, J. J. Kinematic model of a magnetic-microrobot swarm in a rotating magnetic dipole field. IEEE Robot. Autom. Lett., 5(2), 2419–2426, 2020. DOI: 10.1109/LRA.2020.2972857

[17] Tang, X.; Li, Y.; Liu, X.; Liu, D.; Chen, Z.; Arai, T. Vision-Based Automated Control of Magnetic Microrobots. Micromachines 2022, 13, 337. https://doi.org/10.3390/mi13020337

[18] Jialin Jiang , Lidong Yang , Shihao Yang , Li Zhang Deep Learning-based Framework for Environment adaptive Navigation of Size-adaptable Microswarms IEEE Trans. Robot., 37(6), 1890–1905, 2021. DOI: 10.1109/TRO.2021.3078573

[19] Xia, X., et al. Artificial Intelligence-Assisted Multimode Microrobot Swarm Behaviors. ACS Nano, 18, 2024. DOI: 10.1021/acsnano.4c16347

[20] Raissi, M., Perdikaris, P.,& Karniadakis, G. E. Physics-informed neural networks: A deep learning framework for solving forward and inverse problems involving nonlinear PDEs. Journal of Computational Physics, 378, 686–707, 2019. DOI: 10.1016/j.jcp.2018.10.045

[21] Avaneesh, Ritwik & Venezian, Roberto & Kim, Chang & Park, Jongoh & Misra, Sarthak & Khalil, Islam. (2021). Open-Loop Magnetic Actuation of Helical Robots using Position-Constrained Rotating Dipole Field. 10.1109/IROS51168.2021.9636564.

[22] Jingjie Zhou, Side Zeng, Fei Wu, Fangzhi Mou; A navigation system for permanent-magnet-actuated microswarm. Nanotechnol. Precis. Eng. 1 December 2025; 8 (4): 043011. DOI: 10.1063/5.0248657

[23] Sitti, M., Ceylan, H., Hu, W., et al. Biomedical applications of untethered mobile Milli/microrobots. Nature Reviews Materials, 1, 16064, 2015.

[24] Wang, Luyao and Gan, Chunyuan and Sun, Hongyan and Feng, Lin,Magnetic nanoparticle swarm with upstream motility and peritumor blood vessel crossing ability, Nanoscale, 2023, 15, 34, 14227-14237, The Royal Society of Chemistry, DOI: 10.1039/D3NR02610H.